

# Development of a solar diffuse radiation mapping instrument

**Guilherme Barreiro Vieira; B315177**

**Electronic & Electrical Engineering, MEng**

**Abstract:** With the growth of solar resource utilisation, there is a growing necessity for improving the way we model estimations of solar radiation on a tilted plane, due to economic feasibility of installing a new PV system or to assess the performance of existing PV systems. In order to do this, transposition models are used to transpose global horizontal data into separate irradiance components of which the diffuse radiation can sometimes be considered isotropic for simplicity. This project consists of the construction of an instrument capable of scanning the skydome for diffuse radiation in order to map the data and further understand its distribution for different sky conditions. The system is comprised of a two axis movement structure utilising a stepper motor (azimuth position) and a servo motor (zenith position), with a sensor collector tube used to limit the field of view of which a photovoltaic pyrometer is in. The system design methodology is further explained, along with its operation. The results are discussed in relation to the irradiance distribution and correlation between the measured data and the calculated sun positions in order to validate the systems functionality. Finally, the system limitations and improvements are identified and recommendations for further research of the diffuse radiation distribution using this instrument are proposed.

## 1. Introduction

Modelling a new installation of a PV System increasingly requires an accurate evaluation of the solar resource in order for the owner to assess its economic feasibility or to assess its existing PV system performance. Due to the regular unavailability of measured data of the site in scrutiny, transposition models are required to estimate the global irradiance incident in a tilted system plane from global horizontal measurements, available from Meteorological sites nearby. For these models to work they require the separation of different radiation components. These can be divided into the beam component, which comprises of the radiation coming directly from the sun; the diffuse component of radiation is the radiation that has been scattered from molecules in the atmosphere and the albedo component (smallest component) which comprises of the ground reflected radiation. These models can work with some estimations, such as assuming isotropic distribution of the diffuse irradiation component. This approximation reduces the accuracy of these models considerably and efforts to improve its quantification should therefore be pursued.

The following project aims to focus on developing an instrument that can scan the sky for diffuse irradiation. The constructed system will use a photovoltaic pyranometer sensor as it exhibits similar characteristics to a PV cell, with a quick response time and the same spectral response. By mounting it in a two-axis structure, the sensor will be covered by a tube in order to limit its field of view (FOV) that will spin and scan the sky at different angles of incidence in relation to the sun. The data collected will then be mapped through a MATLAB script and the results of the analysis will be presented in this report. A set of objectives were defined to achieve the aims, which are the following:

- Develop sensor circuitry to measure irradiance from a patch of sky.
- Develop the sensor positioning apparatus.
- Develop the motor controller and data logger.
- Sub system integration.
- Data evaluation and visualisation.

## 2. Background Information

### 2.1 Transposition Models

This section will provide some insight into how transposition models work and will briefly review some of the existing models to date. These transposition models often don't use the most optimal input data due to its unavailability for the site

in question, and therefore need to be estimated by transposing the global horizontal irradiance into a tilted system plane, which is available from most Meteorological offices. The more regular the measurements are the more accurate the transposition models become, ergo, having hourly or minute by minute data is more optimal than daily or weekly averages, these will vary depending on where the data was available from. Figure 1 illustrates the different steps taken in the transposition models. These models use irradiance component separation methods using location parameters (longitude and latitude) and a hourly data time series of the solar irradiance in the horizontal plane. From this irradiance component separation, a time series of the diffuse and beam components in the horizontal plane can be extracted which are then utilised to calculate the separate beam component in the tilted system plane by inputting the system plane geometry (tilt and azimuth). As a result, the beam and diffuse components are calculated for the system in plane which are then summed to obtain a time series of the solar total irradiance of the system in plane. From this it is easy to calculate the annual solar radiation in system plane by summing the total irradiance of the system in plane over the entire year.

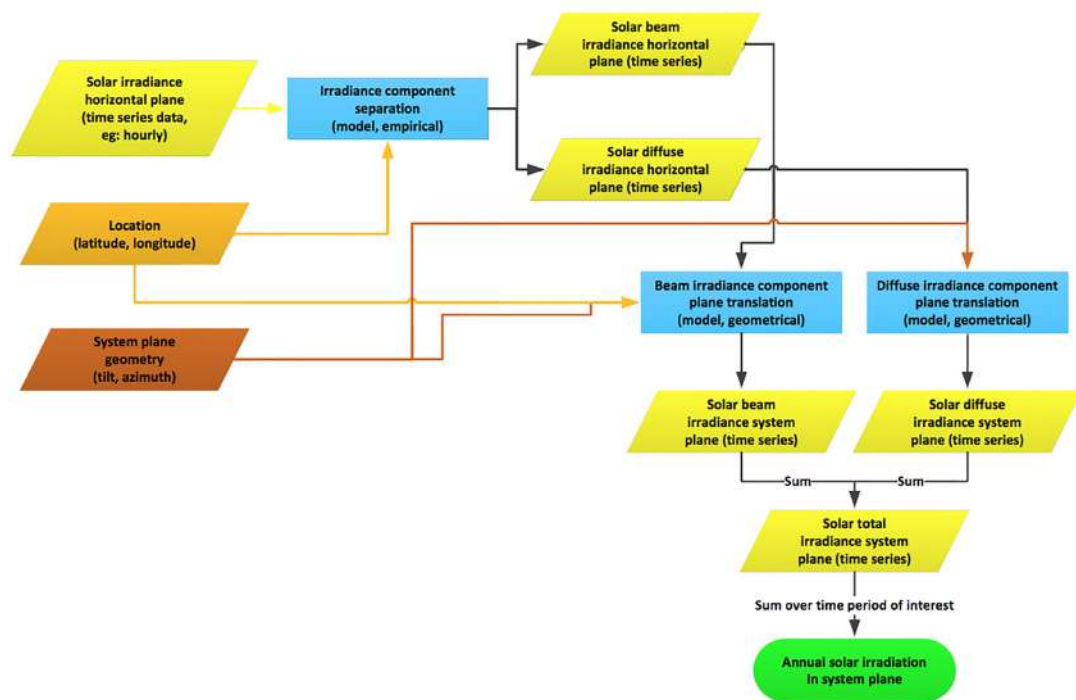


Figure 1 - Diagram illustrating the different steps of transposition models [1].

Literature presents a variety of existing models developed over the years which have been evaluated by [2]. A discussion of the difference between these models is undertaken and a mean absolute difference between the direct measurements in the tilted plane and the models estimations is evaluated. First, these models are presented:

- Isotropic Model (Hottel and Woertz, 1942) is the simplest sky model which assumes that all diffuse radiation is uniformly distributed across the sky as well as assuming the reflection off the ground to be uniform. Hence, it underperforms in relation to any other model due to its simplicity even though it can be considered a relatively good approximation during complete cloud coverage of the sky [2].

$$I_t = I_{h,b} R_b + I_{h,d} \left( \frac{1 + \cos \beta}{2} \right) + I_h Q \left( \frac{1 - \cos \beta}{2} \right) \quad (1)$$

$I_t$  = Total Irradiance in Tilted plane

$R_b$  = Ratio of tilted and horizontal solar beam irradiance

$I_{h,b}$  = Direct normal beam component on horizontal surface

$I_h$  = Global horizontal irradiance,  $\frac{W}{m^2}$

$Q$  = ground reflectance

$\beta$  = Surface tilt angle from horizon, °

- Klucher Model (1979) includes a more detailed parameter, such as horizon brightening and the effect of circumsolar radiation around the sun's position which further improves its accuracy. This model considers a clearness index

parameter which takes into account different sky conditions, however, when the clearness index becomes zero, meaning the sky is completely covered in clouds, it's reduced back to the isotropic model [2].

$$I_t = I_{h,b} R_b + I_{h,d} \left( \frac{1+\cos\beta}{2} \right) \left[ 1 + F' \sin^3 \left( \frac{\beta}{2} \right) \right] \cdot \left[ 1 + F' \cos^2 \theta \sin^3 \theta_z \right] + I_h \rho \left( \frac{1-\cos\beta}{2} \right) \quad (2)$$

- Hay-Davies Model does not take into account the horizon brightening effect but considers an isotropic and circumsolar component of the diffuse radiation. It also adds an anisotropy index 'A' which is a ratio used to quantify the portion of diffuse radiation that is treated as circumsolar in relation to the remaining diffuse radiation being assumed isotropic. Reflection off the ground (albedo element of radiation) is dealt equally to the isotropic model [2].

$$I_t = (I_{h,b} + I_{h,d} A) R_b + I_{h,d} (1-A) \left( \frac{1+\cos\beta}{2} \right) + I_h \rho \left( \frac{1-\cos\beta}{2} \right) \quad (3)$$

- Reindl Model similarly uses the anisotropy index 'A' as the Hay-Davis Model, yet in addition to the isotropic diffuse and circumsolar radiation, it also includes the horizon brightening. Due to this additional term in the equation, this model provides a slight improvement in relation to the Hay-Davies model - slight higher diffuse irradiance. Reflection (albedo component) is again dealt the same way as in the isotropic model. The total irradiance on a tilted surface can be calculated using [1]:

$$I_t = (I_{h,b} + I_{h,d} A) R_b + I_{h,d} (1-A) \left( \frac{1+\cos\beta}{2} \right) \cdot \left[ 1 + \sqrt{\frac{I_{h,b}}{I_h}} \sin^3 \left( \frac{\beta}{2} \right) \right] + I_h \rho \left( \frac{1-\cos\beta}{2} \right) \quad (4)$$

- Munger Model (1997) is slightly more complex and treats shaded and sunlit surfaces separately. An additional parameter 'Tf' representing the ratio of the slope background diffuse irradiance to the horizontal diffuse irradiance' [1]. This anisotropic index is multiplied by the diffuse radiation component. It developed two different equations to calculate total irradiance on a tilted plane for both non-overcast and overcast sky conditions. He also supplies fixed values for the different overcast conditions for Europe locations, and a function of the anisotropic index.
- Perez model (1991) is by far the most complex and more computationally expensive, it takes into account a much more detailed analysis of the diffuse distribution by using coefficients for different sky conditions derived from empirical data. It not only takes into account coefficient for the circumsolar and horizon brightness but also bases these on additional clearness and brightness indexes which are dependant on defined sky conditions. This evidently is the most complex models out of the ones being taken into account and it's calculations will not be demonstrated in this report [4].

Munner and Perez models are by far the most complex and therefore the most accurate existing models to use. Their performances have been evaluated and compared to real measured data and the mean absolute differences for each model have been calculated in [1]. These mean absolute differences were around 13.7-14.9% for the isotropic sky model; 13.2% for the Klucher model; 9.1% for the Hay-Davies model; 9.4% for the Reindl Model; 7.6 % for the Mungers Model; 6.6-9.0% and 7.9% for the 1990 and 1987 Perez models respectively [1]. It is also important to note that these errors can vary significantly depending on the overcast conditions. They generally vary less when calculating for clear-sky conditions due to the irradiance changing slower and in smoother ways due to the open sky, whereas they can become larger when calculating for partly-cloudy conditions as these sky conditions present more irradiance variations at quicker intervals [5].

These results put into contrast the existing errors with the current models used to calculate the total irradiance in a system plane when the separation of irradiance components has been performed. There has been further effort in ameliorating these estimations by classified sky conditions into different categories that are based on empirical data - these can be found in the appendix [Appendix 1].

A study has been conducted in Denmark which similarly aimed to determine or better understand the diffuse angular distribution as well as the effect that clouds have over it. This study used 8 pyrometers inside different domes, each pointing at a different 1/8th of the skydome. The results were then correlated with global diffuse radiation measurements in order to validate them, and a short analysis of the effects of the diffuse fraction radiation distribution in different sky conditions was conducted [6]. Similarly to this study, this project will then aim to contribute to these efforts by creating a

low-cost sky scanner that could be utilised in further researching and validating said models by providing a relatively high resolution mapping of the skydome.

## 2.2 Measuring Instrumentation

There are a few choices in instrumentation for measuring radiation. One of the most abundantly used is thermopile pyrometers (Figure 2a), which are usually used to measure global in-plane diffuse or ground-reflected component of irradiance. Its advantages lies in offering a broader spectral response over other measuring instrumentation, with little reflection over a wide range of angles of incidence. It's disadvantages are derived from its slow response due to the need of the absorber element to heat up in relation to the reference point as well as its price.

A photovoltaic effect sensor (Figure 2b) is essentially a solar cell. It has quite a narrow spectral response as well as being susceptible to reflection errors, however, its benefits lie in the fact that's its characteristics are the same as a PV module, and it has a fast response which offers an improvement in relation to the thermopile pyranometer regards to the application of this project.

The pyrhelimeter (Figure 2d) is an instrument that is used to measure direct beam solar irradiance. It's comprised of a tube with a window which limits the field of view, with a thermopile at the bottom of the tube which converts the heat into an electrical signal that is proportional to irradiance. These are normally placed onto a sun tracker so it can track the suns position in order to measures its direct beam, which makes it substantially more expensive than other measuring devices.

Finally photovoltaic pyranometers (Figure 2c) essentially work the same way a photodiode does. It's current/voltage generated is proportional to the irradiance received. It's response time is quick, in the order of nanoseconds according to the datasheet, and possesses the same spectral response of a solar cell [7].

The requirements of this project sensors lie in a rapid response, price and a similar spectral response to a PV cell, hence, it makes the photovoltaic pyranometer sensor well suited for this application. Finally, its availability at Holywell CREST Laboratory and size made it practical to use with a tube to limit the field of view (FOV) similarly pyrhelimeter. This way, by inserting it in a two-axis movement structure, one can scan the sky for individual measuring points and determine the irradiance distribution across the sky.

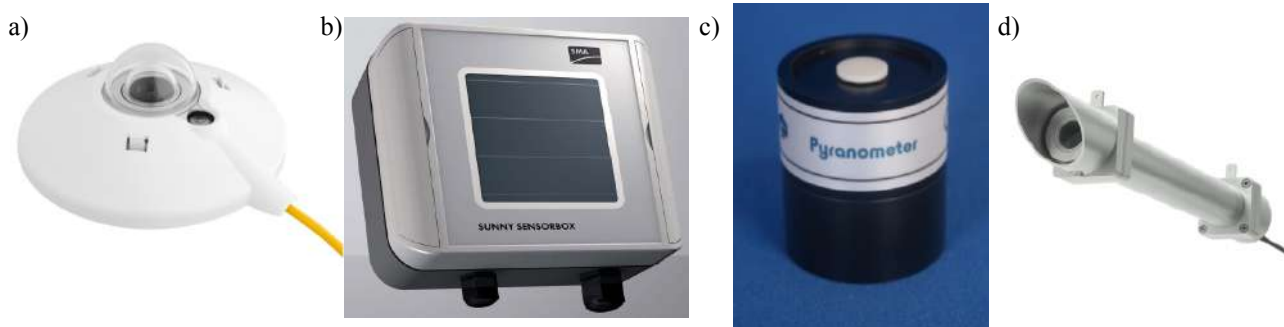


Figure 2 - a) Thermophile pyranometer [1]; b) Photovoltaic Sensor [1]; c) Photovoltaic Pyranometer [7]; d) Pyrhelimeter [8].

## Instrument Build Concepts

This section will discuss briefly the research done in various hardware aspects required to build the instrument.

Research was done in relation to photo detection circuits used to amplify the sensors small signal. A few options were available such as transimpedance amplifier circuits that uses the current output mode of the sensor, as well as a simple non-inverting amplifying circuit that uses the voltage output mode of the sensor. From the transimpedance amplifiers, there were two different types, the photovoltaic mode and photoconductive mode. The photovoltaic mode is used for maximising light sensitivity and linearity (precision applications), whereas the photoconductive mode is more suited for applications that require a fast response to light [9]. The non-inverting amplifying circuit is an option that is simplistic but can work well in certain applications and was found to be used in some pyranometer circuits [10]. The decision of what circuit was chosen is further discussed in sections 3.1.

In regards to the motor options that could be used for the sensor positioning apparatus, three types of motors were reviewed, DC, stepper and servo motors. DC motors are continuous motors that can run at high RPMs and use PWM to control the motor. Servos are essentially a DC motor assembled with gears, control circuit and a position-sensor which enables a more precise control of position, hence making it possible to start and stop at desired locations. They can be fast and have quite a high torque. The stepper motor uses multiple tooth electromagnets that surround the motor which activate and deactivate alternatively making the shaft turn. They rotate in pre-defined steps with fixed angular increments, ergo, the motor moves at a known position for every turn, making it into a more precise motor which often can be run without position feedback if precision is not a requirement or if it's not left running in open loop for a long period of time. The choice of motors was compared to the requirements and will be further discussed in section 3.5.

In order to have precise position feedback, research on encoders was conducted and two main choices were explored, the optical absolute and the mechanical absolute encoder. The optical encoder utilises a disc made of glass/thin metal attached to the rotating shaft with marked transparent areas which are detected by the photodetector array that then reads the pattern imprinted on the disc in order to determine the discs position and direction at any time. The mechanical encoder requires physical contact with the rotational motion and uses a gray code disk in a similar way that the optical encoder does, however the mechanical encoder has a binary code for every single position. It's accuracy is dependent on the patterns that are on the code disc and the rigidity of the mechanical assembly of the device [11].

### 3. Design Methodology

This section comprises of the design process of the system, as well as the methods that were explored and chosen in order to map the skydome appropriately. Firstly, it is important to note the interdependencies in between the design process to better understand the effect the choices made on other parts of the system, which is illustrated in Figure 3. This helps visualise the important steps that were undertaken to advance in the project and the parameters that stalled the development of the system, referred to in the following sections.

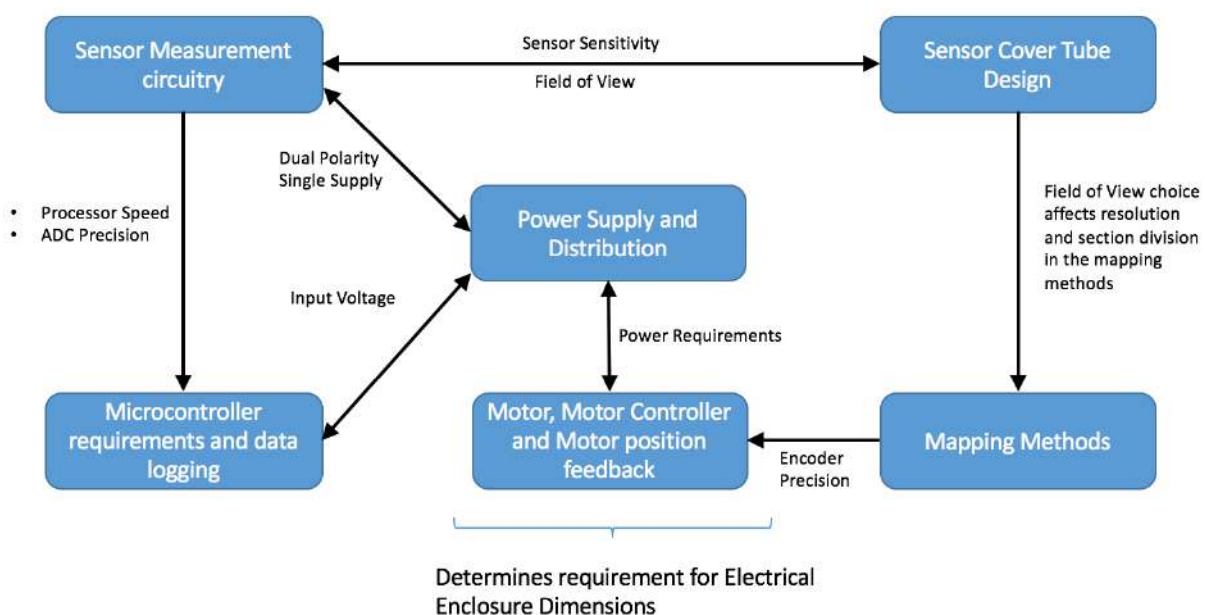


Figure 3 - System Design interdependencies

#### 3.1 Sensor Measurement Circuitry

The amplifying circuit was one of the most challenging subsystems to develop as the sensors voltage output or current output were very small, voltage output was  $10\mu\text{V}/\text{Wm}^2$  and current output was  $46.68\text{ nA}/\text{Wm}^2$  [Appendix 2]. For these reasons the signal needed to be amplified significantly in order to be read accurately. As previously mentioned a few circuits were researched. Taking into consideration that the circuit requires a fast response due to its continuous rotation, the transimpedance photovoltaic mode circuit was not pursued. Hence, the transimpedance amplifier and the basic non-inverting amplifier were explored, illustrated in Figure Circuit. The transimpedance amplifier is one of the most widely

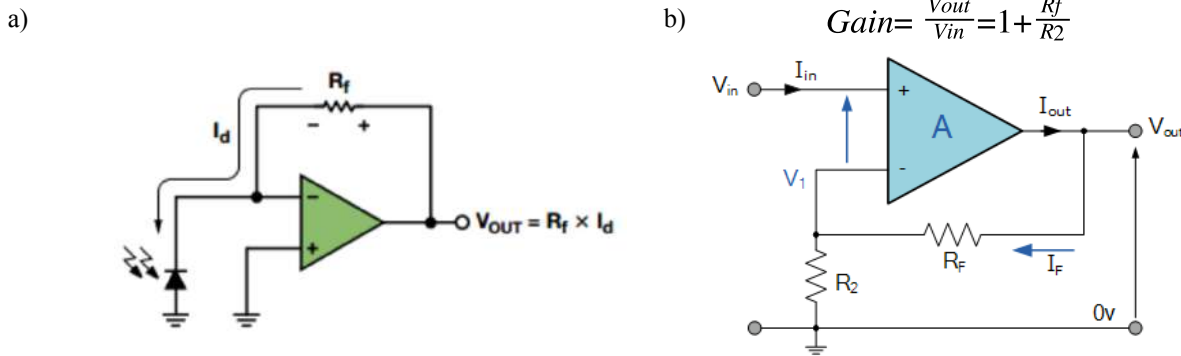


Figure 4 - a) Transimpedance amplifier[12]; b) non-inverting amplifier [13].

used circuits for signal amplification in photodiodes and effectively works by converting the sensor output current into a voltage by simple  $V_{out} = -I \cdot R_f$ . Due to the high impedance of the operational amplifier inputs, the current flows through the feedback resistor which subsequently converts it to a measurable voltage, hence, the feedback resistor defines the 'gain' in this case. The basic non-inverting amplifier circuit shown in Figure Circuit b) works by amplifying the difference in voltage between the two input pins. This amplification is set by the two resistors  $R_f$  and  $R_2$  as described in the Figure Circuit. Initially, both circuits were tested to analyse their performance. By performing a current/voltage sweep of these, a graph was produced in order to better verify their linearity in relation to the input (Figure 5).

By inspection, the gap between the experimental data and theoretical data (what should be obtained), there is a clear larger mismatch in the non-inverting amplifier. Additionally, the fact that the operational amplifier was not able to amplify the voltages below 30  $\mu V$  was a problem. This corresponded up to 3  $W/m^2$  of irradiance which falls in the expected diffuse

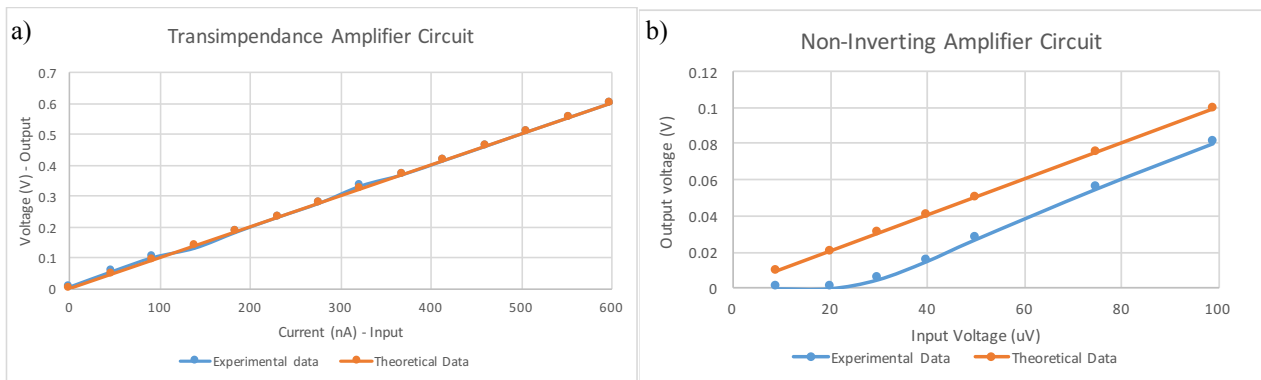


Figure 5 - A comparison of the tested input-output relationship for the transimpedance and non-inverting amplifier circuits.

irradiance, hence limiting the measurement operating range. Furthermore, working with the sensor in voltage output mode, introduces another error parameter which is the input voltage offset. The input voltage offset is 'the differential voltage which must be applied to the input of an op amp to produce zero output' which means that there is always a differential voltage present between the two input pins that shouldn't be there and that is also amplified by the circuit gain [14]. This can be a real problem taking into account that the operating voltages of the circuit are in  $\mu V$  and the input voltage offsets of general purpose precision Op Amps can be between 50-500  $\mu V$ . Moreover, the voltage drift would have also been taken into consideration which is as the name suggests, the amount of voltage that drifts due to changes in temperature. Taking into account that this system is to be placed outdoors, temperature variability would be severe and should therefore be considered. Finally, an operational amplifier with low voltage noise would be required as well as the need for a single supply that facilitated the potential insertion of a battery as a backup power supply [15].

The transimpedance amplifier on the other hand, had a very good response to the small current coming from the sensor even though it was being amplified by a million times. This option removed the problem of the voltage offset as with this circuit the voltage at the input is maintained at 0 V which neutralises leakage currents as well. The requirements for the op

amp in this case would lie in the input bias current which can cause an additional error in the output if too high, a low input offset current, as well as having a low input noise current which inherently affected the SNR of the circuit [16].

Once the set of requirements were established, a higher performance operational amplifier was acquired, the LTC1050 which is a single supply op amp with a low input bias current (30 pA), zero-drift, low voltage noise, low offset current and low input noise current [17].

### 3.2 Microcontroller and Data logger

The Arduino board was used to control the circuit and to do the data logging of the measurements. This was due to its availability and its extensive community which provided libraries that facilitated its use with external add-on modules used, such as the RTC circuit for time keeping and an SD Card for saving the measured data for post measurement analysis. Additionally, an external 16-bit analogue to digital converter (ADC) was purchased in order to measure the voltage of the amplifying circuit more accurately, as the Arduino only contains a 10-bit ADC on the analogue pins which proved to be very noisy and inaccurate when tested [Appendix 3]. A finalised picture of the circuit schematic can be found in [Appendix 4].

### 3.3 Sensor Collector Tube Design

The sensor tube's function in this project was to limit the FOV of the sensor in order for the system to measure equally sized point across the skydome. Limiting the FOV and painting the interior of the tube with a matt black absorbent paint helped remove unwanted light interference reflections coming from different angles of incidence in relation to the tube, this way further ensuring the accuracy in the measurements taken. Additional aperture rings could have been constructed in the tube to prevent further unwanted light interference, however the mechanical workshop of the university was too overloaded with work but should be taken into consideration as an improvement to this design. Furthermore, following the amplifying circuit known responsivity to the sensors output enabled the possibility to define the tube length.

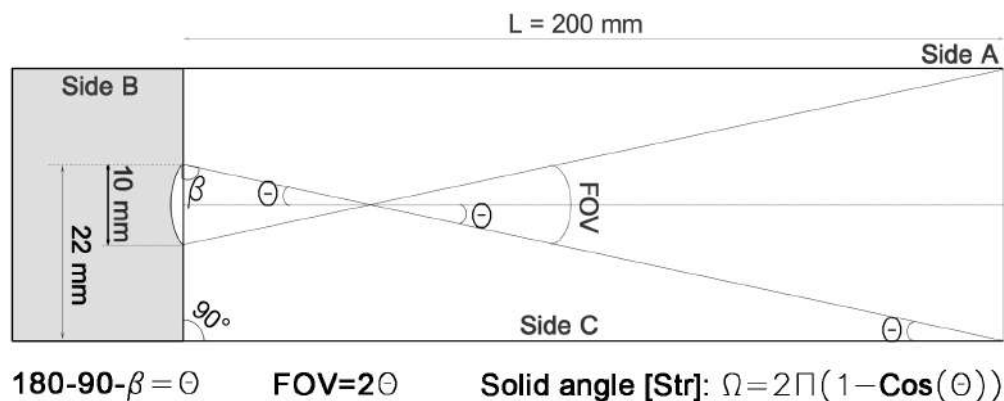


Figure 6 - Sensor collector tube design FOV and solid angle calculations

By using simple trigonometry (Figure 6), the FOV and solid angle were calculated. From these, Table 1 was produced to determine the different FOV angles for different tube lengths in order to estimate the expected irradiance measurements for

Length of Tube (mm)	FOV(degrees )	Azimuth Sections	Solid Angle (Str)	Expected Value for 100 W/m <sup>2</sup> diffuse radiation
200	12.6	28.7	0.038	0.6
190.0	13.2	27.3	0.042	0.66
180.0	13.9	25.8	0.046	0.74
170.0	14.7	24.4	0.052	0.83
160.0	15.7	23.0	0.059	0.93
150.0	16.7	21.6	0.067	1.06
140.0	17.9	20.2	0.076	1.21
130.0	19.2	18.7	0.088	1.40
120.0	20.8	17.3	0.103	1.64
110.0	22.6	15.9	0.122	1.94

Table 1 - Table demonstrating the effect of the length of tube on the FOV, azimuth section division and expected diffuse radiation values



different diffuse irradiance conditions. From the solid angle, a percentage of sky coverage was calculated by simply dividing it by  $2\pi$  (half-sphere) and subsequently multiplied by the different diffuse radiation conditions. Considering that the UK has a relatively cloudy weather, the diffuse fraction of irradiance will normally be quite significant, however, for the sake of designing for the worst case scenario, the values of  $100 \text{ W/m}^2$  of diffuse radiation have been utilised for this decision. Since the transimpedance amplifier responded quite well to low irradiance, the length of 200mm was chosen as it provides a better mapping resolution.

### 3.4 Mapping Techniques

Once the sensor tube length was decided, the section division of the sky-dome could be defined. Two main types of sky-dome configurations were considered. One with equally spaced patches in azimuth and zenith angles but with variant size of patches (Figure 7). The second, with variant spaced patch with equal sized patches [18]. The advantage of the first sky-dome configuration is that the whole sky-dome is covered, however, the variant size of patches make it not suitable for this

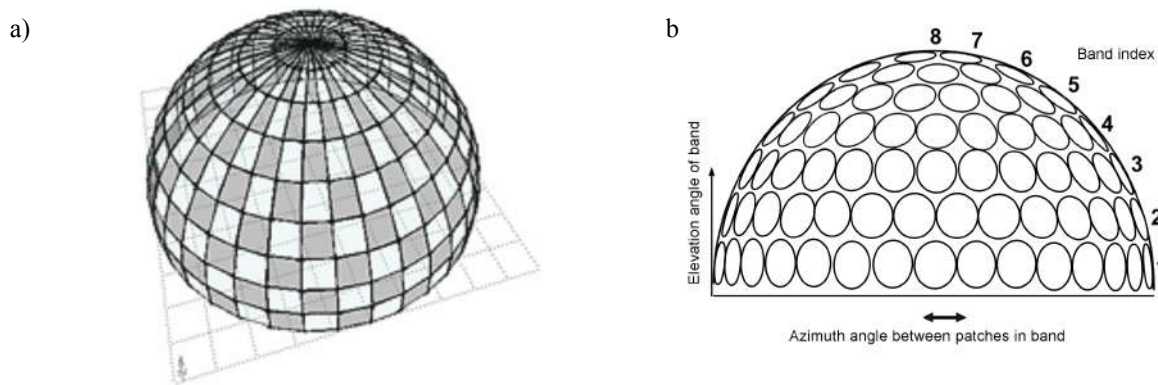


Figure 7 - a) equally spaced patches sky-dome configuration [18] ;b) equally sized patches sky-dome configuration, CIE 145 sky zone [19] - edited.

application as this system has a fixed FOV, hence, making it impossible to change patches sizes along the measurement cycles. The second sky-dome configuration offered the best solution, all the patches are equally sized, but as a trade-off the measurement of the complete sky-dome is compromised due to spaces in between the patches that wouldn't be measured (~90% skydome coverage). This method required the calculation of the arc length of a half sphere at different zenith angles. Since the FOV of 12 degrees was chosen, the sky-dome was divided into 8 zenith sections, and 30 azimuth sections. This can apply for the first zenith row, although the half sphere circumference decreases with increasing zenith angle. Thus, Table 2 shows the calculate section divisions from the calculated arc length for the different 8 bands, which enabled to scale the amount of measuring points that could fit in each band. These calculated values were then tailored to a predefined mapping method also using  $12^\circ$  FOV found in [20] [Appendix 5]. Calculated values for the full range of tube lengths can be found in [Appendix 6].

	1st band ( $6^\circ$ )	2nd band ( $18^\circ$ )	3rd band ( $30^\circ$ )	4th band ( $42^\circ$ )	5th band ( $54^\circ$ )	6th band ( $66^\circ$ )	7th band ( $78^\circ$ )	8th band ( $90^\circ$ )
Paper methodology	30	30	24	24	18	12	6	1.0
Calculated Values	30.0	29.2	26.6	22.8	18.0	12.5	6.4	1.0

Table 2 - Calculated band sections compared to methodology from source [20].

### 3.5 Mechanical Structure

In regards to the structural design of the sensor positioning apparatus, a few design options were developed. This was a student masters projects, hence, the available budget reflected that (£120) which made the design of such a system with so many components challenging. Out of the few design options, the one with the least moving parts and more versatility in



terms of testing was chosen, shown in Figure 8a). Introducing motors to control both angles of movement, enabled a controlled way of scanning the sky-dome as different degrees of movement could be changed by a few simple lines of code. As Figure Dependencies illustrated, due to the tight relationship of the different design variables, this was convenient as for different FOV, a different skydome division was necessary. The reduction of size from Figure 8 a) to b) design was due to budget constraints and to add simplicity to the design, even though it was favourable to have a elevated structure, this could also be achieved by simply placing the structure at a more elevated position, such as a roof of a

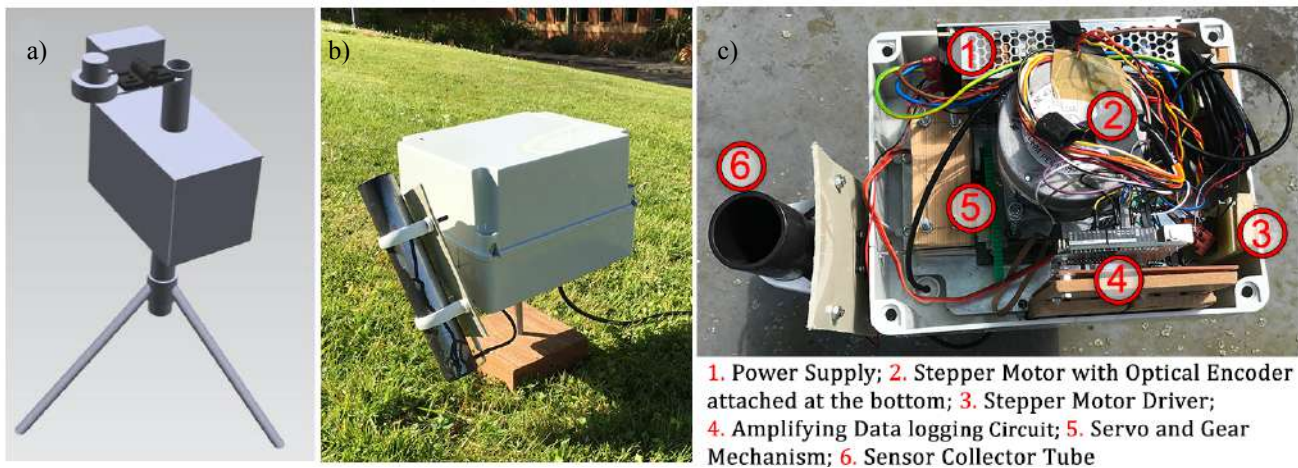


Figure 8 -a) SOLIDWORKS CAD drawing of initial design; b) Finalised system; c) Finalised system interior.

building. Figure 8 c) shows the interior of the system, illustrating how all the subsystems come together. The system is powered from the bottom with a mains adapter so it's easy to disconnect from the mains, however, for additional precaution a panel switch interlock was connected to the power supply so as soon as the box cover is removed, the mains are disconnected. An additional gear mechanism was added so the servo motor wasn't directly connected to the sensor positioning apparatus in case there was an income of water through the hole of which the shaft is connected to the outside. Finally, all the elements were glued to the side of the boxes to avoid drilling in order to maintain the box weather proof.

### 3.5.4 Motor Choice

The motor choice for this project was quite simple due to the availability of a bipolar stepper motor from Holywell Crest Laboratory. This provided an immense cost saving to the system, however, the motor was old and therefore the specifications were inexistent which meant its capabilities were largely unknown, but due to its size and experimentation, by successfully attempting to move heavy loads it would be heavier than the final system, hence determining its viability. A stepper motor moves in distinct steps (1.8 degrees per step) which provides this kind of motor a more predictable position reliability, however, there can be instances of loss of steps, overloading, or stall conditions. As a result, a closed loop position system was introduced by an optical encoder, with a precision of less than 1 angular degree used to prevent for these situations. This way, if there is loss of steps, the encoder will correct and re-synchronise the steps. The reason for the choice of an optical encoder over a mechanical encoder was due to its availability from an old PhD project at Holywell CREST Laboratory, as well as the cost saving factor of having to buy two sets of gears to attach the motor shaft to the mechanical encoder shaft. For the second axis of movement (zenith angle), a servo was chosen due to its ability to easily start and stop at specified angle locations which can prove to be difficult using a DC motor for example. It's cost also added to the design decision as servos are available for a relatively cheap price/inexpensive. A high torque servo of 9.1Kg-cm/91Ncm with metal gears was purchased to prevent any damage from the start and stop momentum force of the sensor positioning arm when the system is operational [21].

## 4. Operation of System

This section will describe the operation of the system and how the system effectively scans the sky following the mapping methods defined in section 3.3. As previously mentioned, there is a different amount of measuring points per band (zenith

angle) which means that the system will measure differently depending on the band that its in. By testing the measuring speed of each valid measurement, one can calculate the time intervals that are needed to take the measurements at the

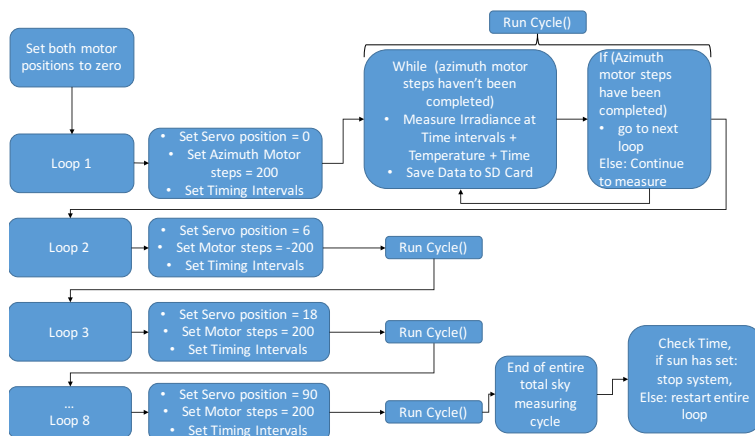


Figure 9 - Flow chart illustrating the code used to scan the skydome.

flow diagram of the operation of the system using the encoder can be found in [Appendix 7]. This method would not be advised to run for a long period of time, as the uncertainties of measurements would increase with the measuring period length.

## 5. Results & Discussion of Collected Data

This section will consist of the presentation of the collected data. A MATLAB script was developed to extract the data from the cvs file (excel) stored in the SD card, separate the data into their respective zenith bands and attribute the different data points different colours in order to plot them in a scatter plot. The plot was modified to look like a wind rose graph to provide a better perception of the measurement positions and to look similar to the chosen skydome configuration - equally sized patches. The outer bands represent the 1st zenith band and the most inner band the 8th zenith band, whereas the azimuth sections are represented by the cardinal directions, South being 0° azimuth, North being 180° and so on. Due to the problem with the optical encoder position, the system was run for short periods of time (15 minutes). Figure Data presents two data sets, one measured in a cloudy day (6pm - 06/05/2017) and the other measured in a partly cloudy day (2pm - 07/05/2017). These measurements were not taken in an open field, but in a garden with obstacles around it due to the need of the system being connected to the mains. By referring to [Appendix 8, 9], a panorama picture of the measurement location in cloudy and partly cloudy conditions respectively provide a better insight of the position of the different obstacles observed in the measurement graphs.

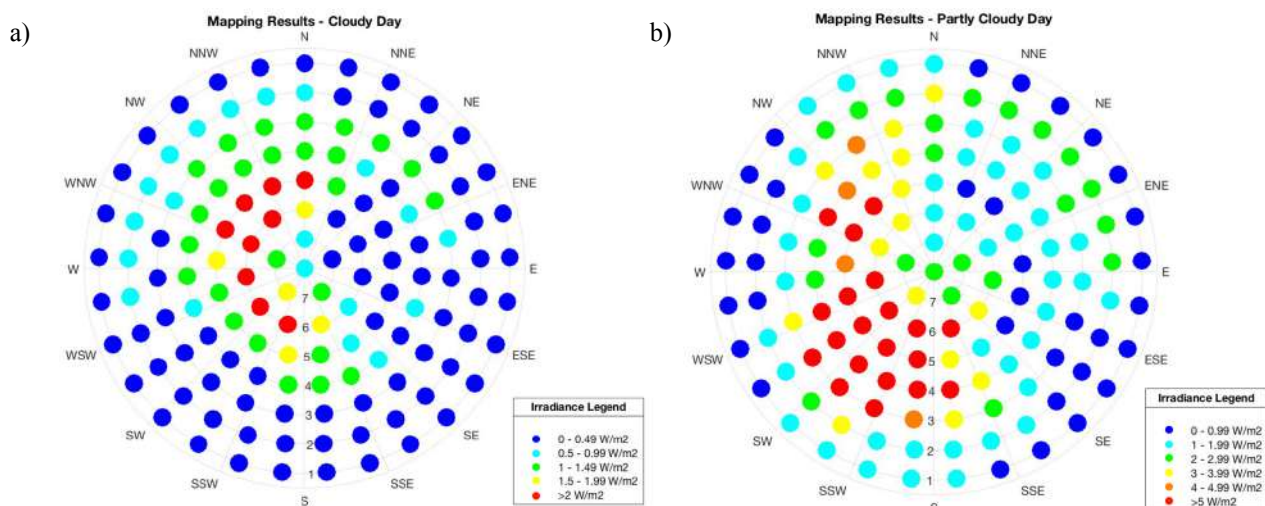


Figure Results - Mapping results for a) Cloudy day (6pm - 06/05/2017); b) Partly Cloudy Day (2pm - 07/05/2017)

Starting with the cloudy day dataset, it is visible that the first couple bands measured very little irradiance due to the sensor position being directed to the wooden fence, however, as the zenith angle increases - inner bands - a more significant irradiance starts to be measured. Due to the fact that this measurement was taken at the end of the day - around 6pm - the higher irradiance measurements are logically positioned towards the west (indicated by the red patches). Due to this being a cloudy day, the overall irradiance distribution is fairly similar considering the difference in colours are of  $0.5 \text{ W/m}^2$ . This confirms the ALL SKY MODEL luminance distribution which states that the more overcast sky, the more uniform irradiance distribution is, as well as the similar study done in Denmark which positions 8 pyrometers in order to verify the diffuse radiation distribution[3][6]. Furthermore, the values obtained within this dataset averaged to about  $0.91 \text{ W/m}^2$  are relatively close to the expected values of  $0.6 \text{ W/m}^2$  if diffuse radiation fraction of 100  $\text{W/m}^2$  assumed for this sky condition. This mismatch is also expected as the dataset average contains the measurements done around the sun's position which should not be included in the diffuse radiation component of solar irradiation.

In regards to the partly cloudy day dataset, a much more colourful graph is presented which reflects a more varied distribution across the sky. Again, the obstacles positioned at SSE and West representing the tree and the wall respectively, show a reduced amount of irradiance represented by the dark blue colour. With increasing zenith angle, the irradiance measurements also increase due to a better line of sight towards the sky irradiance. Due to the time this dataset was taken (2pm), the position of the sun was clearly encountered at around SSW position which matches with the position of the sun at that time of day (calculated in [Appendix 10]). The patches in that area measured up to  $43.8 \text{ W/m}^2$  at azimuth  $60^\circ$  measured in band 4 ( $42^\circ$ ) which closely matches with the calculated azimuth of  $67.97^\circ$  and elevation of  $46.94^\circ$  at this time of day (2pm) and day of the year (07/05/2017).

These results validate the functioning of the system by successfully mapping the skydome, although there were obstacles which served as points of references. To further validate results taken from this system, it would be valuable to compare the sum of all the taken diffuse radiation measurements to direct measurement of the total diffuse radiation taken by the university.

## 6. Limitations of the System

There are some limitations of the system which should be noted. As previously mentioned, the system was designed to operate in between  $-20^\circ\text{C}$  and  $60^\circ\text{C}$  which provides the ability to place it in most geographical locations which would be interested in this kind of device, however, this temperature range has been extrapolated from the data sheets and hasn't been tested against, therefore it should only be operated at a  $\pm 10\%$  of the extremities of this range [Appendix 11].

Furthermore, the system was also designed in order to be weather proof, meaning that the chosen electrical enclosure is IP65 certified, so it is protected against low pressure water jets from any direction. However, the hole of which the side arm is positioned could cause drops of water coming in due to the lack of insulation which could potentially damage the system in rough weather conditions, and should therefore be improved in order to cover for these eventualities.

Furthermore, there is a degree of uncertainty in the measured irradiance accuracy due to the uncertainties of the pyrometer sensor calibration errors (typically less than 3%). Finally, the most significant limitation of the system is its inability to measure the position feedback from the stepper motor (azimuth axis rotation), as it currently repeats angle steps and therefore a full rotation of the motor shaft is not detected by the optical encoder.

## 7. Conclusion

An instrument to scan the sky for diffuse irradiation was developed by following a design methodology which took into account the different interdependencies of the different subsystem requirements. These subsystems were successfully tested and integrated into a mobile system that can be utilised in a wide range of geographical locations, due to its operating temperature range. This system was developed at relatively low cost of £299.56 comparing its industrial equivalent which costs several thousand of pounds with the same measurement resolution (145 measurements)[Appendix 12]. The system was able to fulfil its objectives by mapping the skydome for diffuse irradiance, and the data was demonstrated in equally sized patches of skydome configuration which enabled to measure 90% of the skydome irradiance. Although the encoder sensor for position feedback wasn't fully operational, an alternative method of which the results of the expected sun position was successfully correlated with the calculated sun position in two different sky conditions (cloudy day and partly cloudy day) at the measured time and day of the year. The results have demonstrated the initial purpose of the study, which comprised of proving the anisotropic distribution of diffuse irradiation. For a more detailed analysis, further measurements should be undertaken at multiple sky conditions in order to better determine the

effect of clouds in the irradiance distribution, hopefully contributing and validating the existing transposition models. From this extended datasets, coefficients of different sky conditions could be derived from empirical data such as has been done with the ALL SKY MODEL. Additionally, the measurement accuracy of the system should be tested by correlating the sum of the diffuse radiation measurements with a global horizontal diffuse irradiance measurement from Holywell CREST equipment. Finally, adding a 360 camera on top of the system in order to be able to compare sky conditions with the measurements taken will be beneficial for the data analysis.

## References

- [1] - T. Betts: "Solar Resource Lecture", 16ELP33META Module Notes, School of Electronic, Electrical and Systems Engineering, Loughborough University, 2016-2017.
- [2] - P. Loutzenhiser, H. Manz, C. Felsmann, P. Strachan, T. Frank and G. Maxwell, "Empirical validation of models to compute solar irradiance on inclined surfaces for building energy simulation", *Solar Energy*, vol. 81, no. 2, pp. 254-267, 2007.
- [3] - Igawa, H. Nakamura and K. Matsuura, "Sky luminance distribution model simulation of daylit environment"
- [4] - R. Perez, R. Seals and J. Michalsky, "To all-weather model for sky luminance distribution—preliminary configuration and validation", *Solar Energy*, vol. 51, no. 5, p. 423, 1993.
- [5] - C. Gueymard, "FROM GLOBAL HORIZONTAL TO GLOBAL TILTED IRRADIANCE: HOW ACCURATE ARE SOLAR ENERGY ENGINEERING PREDICTIONS IN PRACTICE", *American Solar Energy Society*, 2017.
- [6] - E. Andersen, K. Nielsen, J. Dragsted and S. Furbo, "Measurements of the Angular Distribution of Diffuse Irradiance", *Energy Procedia*, vol. 70, pp. 729-736, 2015.
- [7] - "SKS 1110 PYRANOMETER", Skye Instruments Ltd, Powys, 2017.
- [8] - "DR01 pyrheliometer | Hukseflux", *Hukseflux.com*. [Online]. Available: <http://www.hukseflux.com/product/dr01-pyrheliometer>. [Accessed: 08- May- 2017].
- [9] Microchip, "Using a Digital Potentiometer to Optimize a Precision Single-Supply Photo Detection Circuit", Microchip Technology Inc., 2004.
- [10] - "Example circuit of LM35 temperature sensor and a chopperless DC amplifier for Pyranometer - Basic\_Circuit - Circuit Diagram - SeekIC.com", *Seekic.com*, 2013. [Online]. Available: [http://www.seekic.com/circuit\\_diagram/Basic\\_Circuit/Example\\_circuit\\_of\\_LM35\\_temperature\\_sensor\\_and\\_a\\_chopperless\\_DC\\_amplifier\\_for\\_Pyranometer.html](http://www.seekic.com/circuit_diagram/Basic_Circuit/Example_circuit_of_LM35_temperature_sensor_and_a_chopperless_DC_amplifier_for_Pyranometer.html). [Accessed: 08- May- 2017].
- [11]- E. Eitel, "Basics of Rotary Encoders: Overview and New Technologies", *Machine Design*, 2015. [Online]. Available: <http://www.machinedesign.com/sensors/basics-rotary-encoders-overview-and-new-technologies-0>. [Accessed: 08- May- 2017].
- [12] - L. Orozco, "Optimizing Precision Photodiode Sensor Circuit Design", *Analog Devices*, vol. -2624, 2014.
- [13] - "Non-inverting Operational Amplifier - The Non-inverting Op-amp", *Basic Electronics Tutorials*. [Online]. Available: [http://www.electronics-tutorials.ws/opamp/opamp\\_3.html](http://www.electronics-tutorials.ws/opamp/opamp_3.html). [Accessed: 08- May- 2017].
- [14]"Op Amp Input Offset Voltage", *Analog Devices*, vol. -037, 2008.
- [15] - J. Karki, "<http://www.ti.com/lit/an/sloa011/sloa011.pdf>", *Mixed Signal and Analog Operational Amplifiers*, vol. 011, 1998.
- [16]-H. Hashemi, "Transimpedance Amplifiers (TIA): Choosing the Best Amplifier for the Job", *Texas Instruments*, vol. 942, 2015.
- [17]-Linear Technology, "LTC1050 Precision Zero-Drift Operational Amplifier with Internal Capacitors", Linear Technology, 2017.
- [19]-B. Goss, I. Cole, T. Betts and R. Gottschalg, "Irradiance modelling for individual cells of shaded solar photovoltaic arrays", *Solar Energy*, vol. 110, pp. 410-419, 2014.
- [18]"Sky Subdivision | Natural Frequency", *Naturalfrequency.com*, 2011. [Online]. Available: <http://naturalfrequency.com/wiki/sky-subdivision>. [Accessed: 08- May- 2017].
- [20]M. Bodart, A. Deneyer, A. De Herde and P. Wouters, "Design of a new single-patch sky and sun simulator", *Lighting Research and Technology*, vol. 38, no. 1, pp. 73-89, 2006.
- [21]"Particular Specification", *hphobbies*, 2005. [Online]. Available: <https://www.bphobbies.com/pdf/BMS-620MG.pdf>. [Accessed: 08- May- 2017].



## Appendix

## Appendix 1

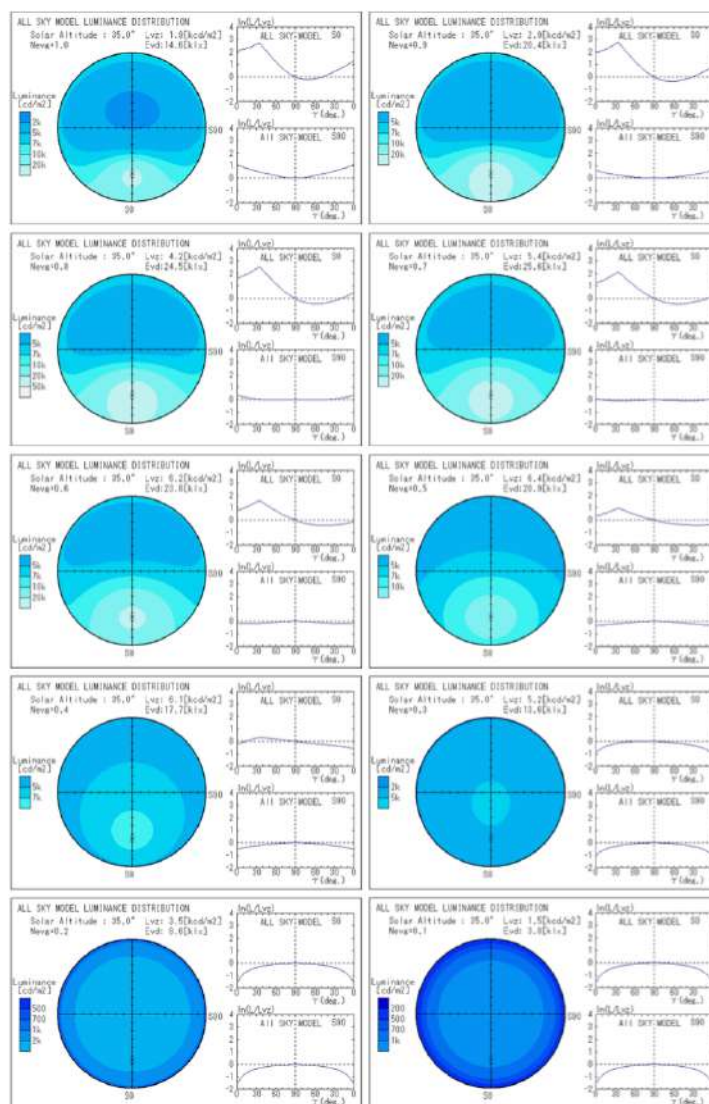
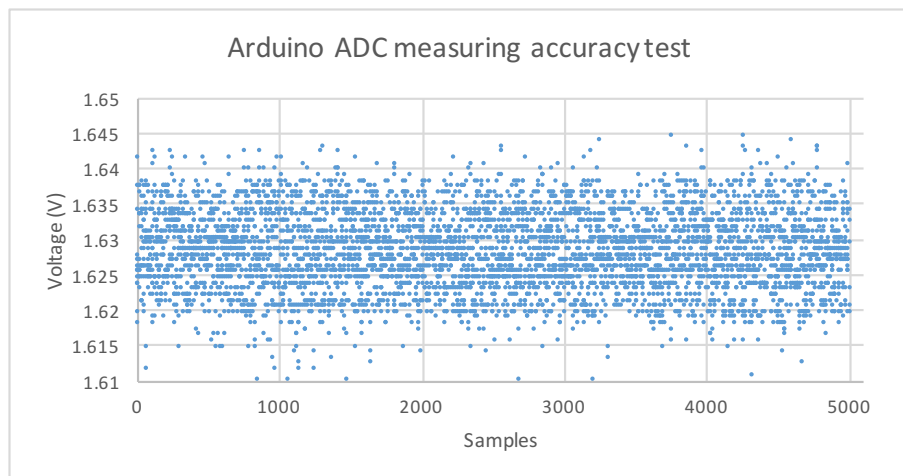


Fig.6 Absolute value of sky luminance distribution from clear sky to overcast sky (Solar Altitude: 35deg.)

## Appendix 2

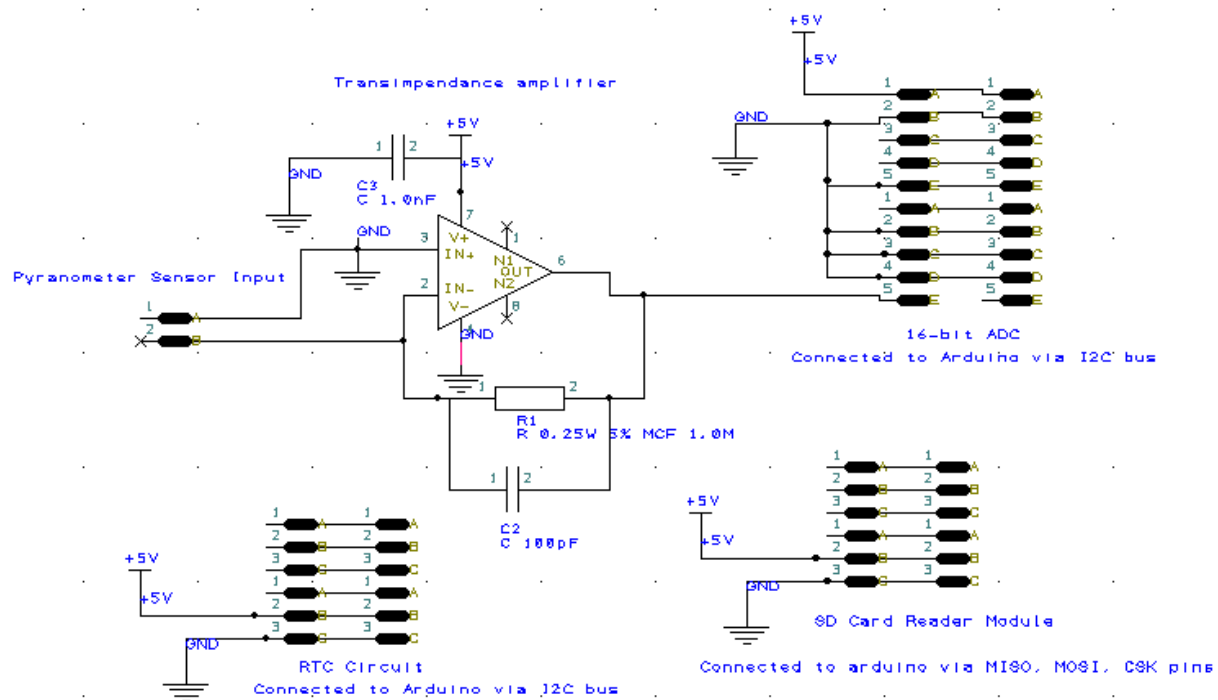


## Appendix 3



Arduino ADC measuring accuracy test when feeding in 1.65V from power supply. The average measured voltage was of 1.625-1.63V.

## Appendix 4



## Appendix 5

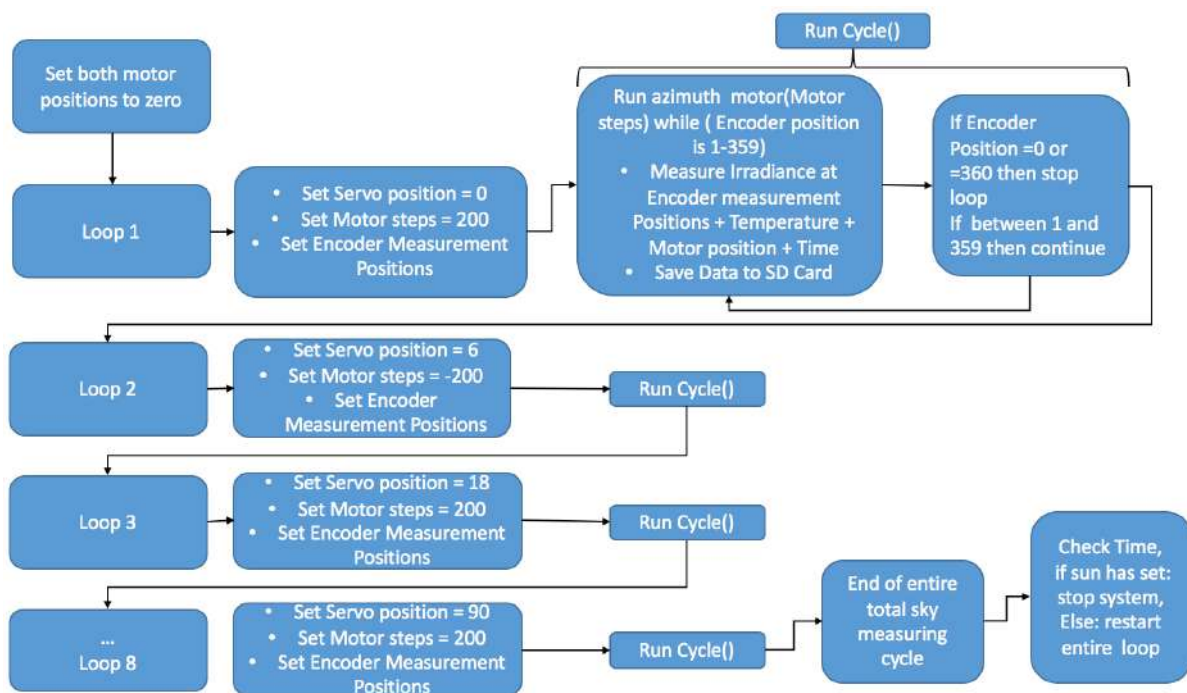
Strip	Elevation angle (horizon = 0°) [°]	Number of patches	Horizontal angle between the patches [°]	Weighting factor = (1 + 2sinE)/3
1	6	30	12	≈0.403019
2	18	30	12	≈0.539345
3	30	24	15	≈0.666666
4	42	24	15	≈0.779420
5	54	18	20	≈0.872678
6	66	12	30	≈0.942364
7	78	6	60	≈0.985432
8	90	1	—	1

## Appendix 6

			1st band	2nd band	3rd band	4th band	5th band	6th band	7th band	8th band	
Tube length	FOV(degrees)	Arc length	No. Sections	No. Sections	No. Sections	No. Sections	No. Sections	No. Sections	No. Sections	No. Sections	Total Sections - Resolution
20	12	0.205	30.0	29.2	26.6	22.8	18.0	12.5	6.4	1.0	146.4
19	13	0.222	27.7	26.9	24.5	21.0	16.6	11.5	5.9	1.0	135.2
18	14	0.239	25.7	25.0	22.8	19.5	15.4	10.7	5.5	1.0	125.6
17	14.5	0.248	24.8	24.1	22.0	18.9	14.9	10.3	5.3	1.0	121.3
16	16	0.273	22.5	21.9	19.9	17.1	13.5	9.3	4.8	1.0	110.0
15	17	0.290	21.2	20.6	18.7	16.1	12.7	8.8	4.5	1.0	103.6
14	18	0.307	20.0	19.4	17.7	15.2	12.0	8.3	4.2	1.0	97.9
13	19	0.324	19.0	18.4	16.8	14.4	11.4	7.9	4.0	1.0	92.8
12	21	0.358	17.1	16.7	15.2	13.0	10.3	7.1	3.6	1.0	84.1
11	22.5	0.384	16.0	15.6	14.2	12.2	9.6	6.6	3.4	1.0	78.5

Table demonstrating the calculation results for the azimuth section division for different tube lengths.

## Appendix 7





Appendix 8



Appendix 9 -



**Appendix 10 - Calculations for Sun position of 7th of May****Hour angle:**

$$\omega = (t - 12)15 \quad \text{for 2 pm, } t = 14$$

$$\text{So } \omega = 30$$

**Solar Declination:**

$$\delta(^{\circ}) = 23.45 \sin\left(\frac{360}{365} \times (DoY + 284)\right)$$

Since 7th of May is 127th day of the year  
Solar Declination = 16.688

**Sun Elevation angle:**

$$\sin(h) = \sin(\delta)\sin(\phi) + \cos(\delta)\cos(\phi)\cos(\omega)$$

By substituting solar declination, Latitude (52.76 for Loughborough) and hour angle,  $h = 46.94^{\circ}$

**Sun Azimuth angle :**

$$\cos(\zeta) = \frac{\sin(h)\sin(\phi) - \sin(\delta)}{\cos(h)\cos(\phi)}$$

By substituting calculated solar elevation, solar declination, and latitude, azimuth angle was found to be =  $67.98^{\circ}$

**Appendix 11**

Operating temperature of the different hardware components:

- LTC1050 :  $-40^{\circ}\text{C}$  to  $85^{\circ}\text{C}$  degrees (Source: [17])
- Arduino :  $-40^{\circ}\text{C}$  to  $85^{\circ}\text{C}$  degrees (Source: <https://www.digchip.com/datasheets/parts/datasheet/1848/A000049.php>)
- Motor stepper driver :  $-20^{\circ}\text{C}$  to  $85^{\circ}\text{C}$  (Source: [https://www.pololu.com/file/download/a4988\\_DMOS\\_microstepping\\_driver\\_with\\_translator.pdf?file\\_id=0J450](https://www.pololu.com/file/download/a4988_DMOS_microstepping_driver_with_translator.pdf?file_id=0J450))
- Stepper Motor : Unknown
- Servo motor :  $-20^{\circ}\text{C}$  to  $60^{\circ}\text{C}$  (Source: <https://www.bphobbies.com/pdf/BMS-620MG.pdf>)
- Optical sensor HEDS 9000 :  $-40^{\circ}\text{C}$  to  $100^{\circ}\text{C}$  (Source: <https://www.broadcom.com/products/motion-control-encoders/incremental-encoders/transmissive-encoders/heds-9000u00>)
- Pyranometer :  $-35^{\circ}\text{C}$  to  $+75^{\circ}\text{C}$ . (Source: [7])
- Interlock :  $-40^{\circ}\text{C}$  to  $+85^{\circ}\text{C}$  (Source: <https://www.rapidonline.com/cherry-e79-41b-panelswitch-momentary-cheat-interlock-q-c-terminal-6-3-x-0-8mm-50-2669>)
- Power supply :  $-20^{\circ}\text{C}$  to  $70^{\circ}\text{C}$  (Source: <http://uk.farnell.com/tdk-lambda/ls100-12/psu-enclosed-12v-100w/dp/1657452>)

## Appendix 12

Component	Price
Neutrik NAC3MPX powerCON TRUE1 Male Chassis Connector	£3.16
Neutrik NAC3FX-W powerCON TRUE1 Locking Female Cable Connector	£7.23
Bourns Incremental Encoder 120rpm Flatted 5 V	£30.10
Cherry E79-30A Panelswitch, Momentary Cheat Interlock, Q.C. Terminal 4,8 x 0,5mm	£7.28
Bluebird BMS-620MG Double Ball Bearing Metal Gear Servo	£12.89
Power Supply 12V DC 105 W	£22.71
ADS1115 16-Bit ADC - 4 Channel with Programmable Gain Amplifier	£17.90
tinxi® Micro Storage modules Micro SD TF Card Memory Shield Module SPI For Arduino	£4.67
SanDisk Ultra Android 16 GB microSDHC	£5.89
Arduino UNO	£18.65
Optical Encoder wheel	£28.60
HEDS 9000	£19.91
RS Pro Unipolar Hybrid Stepper Motor 1.8°, 1200mNm, 3 V dc, 2 A, 8 Wires	£77.25
Electrical Enclosure	£30.99
RTC Circuit	£1.99
LTC1050 Op Amp	£3.605
Total Cost	£292.83